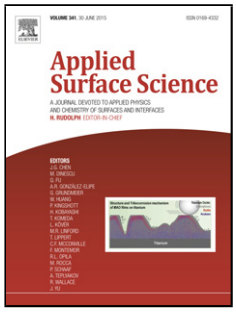

Title: Redox behavior of a low-doped Pr-CeO_2(111) surface. A DFT+U study

Author: <ce:author id="aut0005" author-id="S0169433216329890-d215e6c532e26e876a65e1d273bde7e4"> Brian Milberg<ce:author id="aut0010" author-id="S0169433216329890-b66cc82c8c7d6f5e294a34a60a4a4ea9"> Alfredo Juan<ce:author id="aut0015" author-id="S0169433216329890-61693082906a208c98b44dc02b18c53d"> Beatriz Irigoyen

PII: S0169-4332(16)32989-0
DOI: http://dx.doi.org/doi:10.1016/j.apsusc.2016.12.245
Reference: APSUSC 34792

To appear in: *APSUSC*

Received date: 18-11-2016
Revised date: 26-12-2016
Accepted date: 31-12-2016

Please cite this article as: Brian Milberg, Alfredo Juan, Beatriz Irigoyen, Redox behavior of a low-doped Pr-CeO2(111) surface.A DFT+U study, Applied Surface Science http://dx.doi.org/10.1016/j.apsusc.2016.12.245

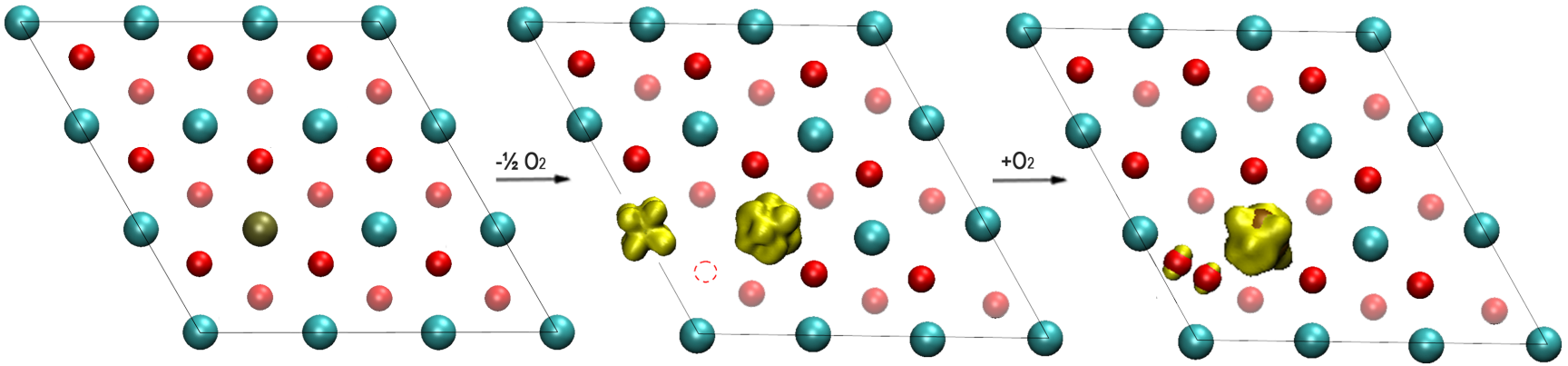

Front view of the 3.7% Pr-doped Ceria(111) surface

The surface with an oxygen vacancy: spin polarization of Ce(3+) and Pr(3+) cations.

The surface with a dioxygen molecule adsorbed above an anionic vacancy: spin polarization of the resulting superoxide species and Pr(3+) cation

Highlights

- Pr doping facilitates oxygen donation due to the easy formation of Pr^{3+}/Pr^{4+} and Ce^{3+}/Ce^{4+} redox couples.
- Pr doping also favors the formation of superoxide (O_2^-) radicals on surface O-holes.
- CO can be oxidized by superoxide radical forming a CO_2 molecule floating on the surface.
- CO can also interact on the (O_2^-)/Pr^{3+} interphase and forms weakly adsorbed carbonate-type intermediates.

Redox behavior of a low-doped Pr-CeO_2(111) surface. A DFT+U study

Brian Milberg[1], Alfredo Juan[2], Beatriz Irigoyen[1]*

[1]ITHES, UBA-CONICET. Departamento de Ingeniería Química, Pabellón de Industrias, Ciudad Universitaria. (1428) Buenos Aires, Argentina.

[2]Departamento de Física & IFISUR, UNS-CONICET. Avda. Alem 1253. (8000) Bahía Blanca, Argentina.

* Corresponding author. E-mail: beatriz@di.fcen.uba.ar

Keywords: DFT+U; Pr-doped CeO_2; redox capacity; dioxygen radicals.

Abstract

In this work, we investigated the redox behavior (donation and replenishing of oxygen) of a low praseodymium (Pr)-doped CeO_2(111) surface. We considered a 3.7 at% Pr doping and performed density functional calculations using the GGA formalism with the 'U' correction on Ce(4f) and Pr(4f) orbitals. Our results indicate that Pr doping promotes oxygen donation by lowering the energy necessary to form surface anionic vacancies. When the $Ce_{0.963}Pr_{0.037}O_2$(111) surface donates one oxygen, the two excess electrons locate on Pr and Ce cations and reduce them to Pr^{3+} and Ce^{3+} ones. Praseodymium doping also favors the activation of O_2 molecule on surface O-holes, leading to formation of a superoxide (O_2^-) radical as well as to reoxidation of the Ce^{3+} cation to Ce^{4+} one. Additionally, we used the CO molecular adsorption for testing the reactivity of those superoxide species. The calculations expose the ability of these radicals to oxidize CO forming a CO_2 molecule floating on the surface. However, when the superoxide is in the immediate vicinity of Pr dopant a carbonate-type species is formed. Our theoretical results may help to gain insight into redox properties and improved catalytic performance of low-doped Pr-CeO_2 solids.

1. INTRODUCTION

Cerium oxide has been extensively employed in environmental applications and heterogeneous catalysis for sustainable energy production [1]. Ceria (CeO_2) participates in the formulation of three-way catalysts, electrodes for solid oxide fuel cells, catalysts for water gas shift (WGS), CO preferential oxidation (COPROX) reactions, and so forth.

The catalytic performance of ceria has been related to its high oxygen storage capacity (OSC). This feature is mainly attributed to an easy oxygen donation, which is originated by the ability of Ce cation to change its formal oxidation state from Ce^{4+} to Ce^{3+}. Moreover, the addition of transition or rare earths metals to CeO_2 leads to materials with improved OSC and redox properties, better thermal stability, and high ionic conductivity and low-temperatures-catalytic activity [2-9].

Regarding redox properties of CeO_2-based materials, it has been reported that the energy required for oxygen vacancies formation strongly depends on the dopants ionic radius [10]. Therefore, it is generally accepted that doping with metals of ionic radius lower than that of Ce cation results in distortions of the fluorite structure with an increase in ceria reducibility [11]. In this regard, CeO_2-ZrO_2 solid solutions have shown high OSC and improved catalytic activity under both oxidant and reducing conditions [2–5,12].

On the other hand, both the small size of Mn^{4+} cations and the presence of (Mn^{3+}/Mn^{4+}) redox couples have been linked to a facilitation for the formation of oxygen vacancies in Mn-doped CeO_2 materials [11,13]. Recently, it has been reported that addition of Pr, a multivalent f-element of similar ionic radius than Ce cation, to CeO_2 results in materials with a fluorite structure like that of ceria and enhanced oxygen storage capacity [9,11]. The improvement of both formation and migration of oxygen vacancies in Pr-doped CeO_2 oxides has been attributed to the presence of (Pr^{3+}/Pr^{4+}) redox couples [14–16]. Notably, these materials have shown a promising catalytic behavior in oxidation reactions such as COPROX and WGS reactions [8,9].

It is recognized that fast refilling of anionic vacancies, originated by oxygen donation during oxidation reactions, is necessary to maintain the high catalytic activity of metal-oxide materials. Thus, activation of O_2 through its adsorption and/or incorporation in the crystal network is considered an essential function of oxide-based catalysts. Even more, it is considered that active oxygen species exhibits higher reactivity than lattice O^{2-} anions and, thus, these species would play a key role during oxidation reactions [17]. Accordingly, superoxide (O_2^-) and peroxide (O_2^{2-}) are two of the most important oxygen species involved in oxidation reactions.

Concerning CeO_2, it has been reported from experimental studies that formation of active oxygen species is strongly influenced by the presence of surface oxygen vacancies [17,18]. There are also some theoretical reports about the effect of metal dopants on oxygen activation on CeO_2–based catalysts. On this subject, DFT calculations have shown the formation of peroxide species (O_2^{2-}) on the clean CeO_2(110) surface while that of

superoxide (O_2^-) on the Au-doped CeO_2(110) one [19]. For Mn–doped CeO_2(111) surface, it has been concluded from DFT+U studies that Mn facilitates not only oxygen donation but also O_2 adsorption, which could be effectively activated to form superoxide (O_2^-) and/or peroxide species (O_2^{2-}) [20].

The production of H_2 mainly involves previous generation of syngas, a mixture of CO and H_2, which is followed by the WGS reaction to transform CO into more hydrogen. Regarding the H_2 stream fed to fuel cells, the oxidation of CO is a crucial step for reducing its concentration to desirable levels to avoid poisoning of the electrocatalysts. In this sense, CeO_2-based catalysts have shown high activity towards CO oxidation mainly due to their high redox activity (Ce^{3+}/Ce^{4+}) and oxygen storage capacity. As well, Pr- and Sn-doped ceria mesoporous flowerlike materials have shown high reactivity on CO oxidation reactions [21].

Despite experimental data indicated that Pr-doped CeO_2 oxides have improved OSC and catalytic behavior in COPROX and WGS reactions, as far as we know, there are no comprehensive fundamental studies about the redox behavior of these materials. Considering that superoxide species are more active than peroxides one in oxidation reactions at low temperatures, we also underline the lack of fundamental studies about the role of activated oxygen species in CO oxidation on Pr-doped CeO_2 catalysts.

Therefore, in the present work we carry out first-principles calculations to model the catalytic behavior of a low praseodymium (Pr)-doped CeO_2(111) surface. For this purpose, we performed density functional theory calculations (DFT) with the Ab-Initio Simulation Package (VASP). We analyzed the geometrical and electronic structures of the Pr-doped CeO_2(111) surface and investigated the beneficial effect of Pr in surface oxygen donation, through calculations of the energy required for creation of oxygen vacancies. We also considered molecular oxygen adsorption on the O-holes. The formed O_2 species were characterized through computation of O–O distances, vibration frequencies and magnetic moments. Finally, we studied the reactivity of these species by using CO as a testing molecule and investigated their role in CO oxidation to CO_2.

2. THEORETICAL METHODS

2.1 The Ideal Solid Model

In this work, we investigated the redox behavior of a low praseodymium (Pr)-doped cerium oxide. The similarity of Ce^{4+} and Pr^{4+} ionic radius (0.96 Å and 0.97 Å, respectively [22]) could facilitate Ce substitution by Pr into the ceria matrix and lead to formation of a

solid solution [23–25]. A series of $Ce_xPr_{1-x}O_{2-\delta}$ samples, with x values in the range [0.99 – 0.80], were greatly crystalized due to the formation of solid solutions caused by the complete insertion of Pr into the CeO_2 crystal lattices [23]. For cerium−praseodymium oxide nanocrystals, X-ray diffraction (XRD) results confirmed the successful incorporation of praseodymium into the ceria lattice forming solid solutions [24]. Substitution of Ce by Pr in $Ce_{1-x}Pr_xO_{2-\delta}$ oxides promoted the Ce^{4+}/Ce^{3+} and Pr^{4+}/Pr^{3+} redox behavior as indicated by the X-ray photoelectron spectra (XPS) analyses [25]. Indeed, XRD characterization of the ceria samples with Pr loadings lower than 15 at% (atomic percentage) prepared in our laboratory has revealed an increase of the lattice parameter [9], which is consistent with formation of solid solutions [26,27]. Changes in the lattice parameters of fluorite type MO_2 oxides (like cerium oxide) due to the formation of solid solutions were predicted by proposed empirical equations; which show the generalized relationship between dopant size and ionic conductivity in the binary systems of these oxides [25]. Electron diffraction patterns obtained for ceria nanoparticles indicated a dependency of lattice parameters estimated by the least squares method on crystalline particle sizes [26]. Besides, it is worthy to note that there is no experimental evidence that Pr oxides (such as Pr_2O_3 or Pr_6O_{11}) were present in the ceria samples synthesized with 5, 10 and 15 at% of Pr dopant [9]. Thus, in this work we focused in modeling the behavior of a cerium-praseodymium oxide solid solution with low content of Pr dopant.

Cerium oxide has a cubic structure of fluorite-type formed by four Ce cations and eight O anions, while the reported experimental value for its lattice parameter is 5.41 Å [28]. The optimization of this structure, within a plane wave basis cutoff energy of 480 eV, led to a calculated lattice constant value of 5.50 Å. Then, we constructed the model of CeO_2 surface by cleaving the optimized bulk cell with the (111) plane and retained an extra oxygen layer. We choose the (111) plane because it is the most stable among the low-index (111), (110) and (100) ones, and corresponds to minimal Ce–O bonds cleavage [29–31].

Therefore, the low-doped Pr-ceria surface model was obtained from a CeO_2(111) slab, with a p(3x3) expansion of the surface unit cell, by substituting one surface Ce cation by Pr. This substitution allowed us to build the 3.7 at% Pr-doped CeO_2(111) surface.

Besides, experimental characterization (X-ray diffraction patterns) of $Pr_xCe_{1-x}O_{2-\delta}$ samples with Pr contents from 5 at% to 15 at% resulted in a lattice parameter value of 5.44 Å [9]; which represents a variation of about 0.6% with respect to the 5.41 Å reported for the bulk structure of undoped ceria. According with these facts we corrected the

calculated bulk lattice constant of undoped CeO_2 as to model the $Ce_{0.963}Pr_{0.037}O_2$(111) surface considering the available experimental information.

In order to perform the energetic analysis, we employed a $Ce_{0.963}Pr_{0.037}O_2$(111) slab with 9 atomic layers and an empty space of 18 Å; which was introduced to avoid periodic interactions with the atoms of the upper image. Besides, we allowed to fully relax all atomic coordinates of those Ce, Pr and O ions located in the six uppermost layers of the slab; while kept fixed the coordinates of those ions placed in the three bottom layers.

2.2 Calculation Methods

First principles calculations were carried out with the framework of density functional theory (DFT) as implemented in the Vienna Ab-initio Simulation Package (VASP) [32,33]. The core electrons were represented with the projector augmented wave (PAW) method [34], and the Kohn-Sham equations were solved with the generalized gradient approximation (GGA), and the exchange-correlation functional of Perdew-Burke-Ernzerhof (PBE) [35]. For electronic wave functions, the cutoff energy of the plane wave basis was set to 480 eV. We also used the Ce($5s^2$, $5p^6$, $6s^2$, $5d^1$, $4f^1$), Pr($5s^2$, $5p^6$, $6s^2$, $5d^1$, $4f^2$) and O($2s^2$, $2p^4$) configurations for valence electrons.

Concerning the $Ce_{0.963}Pr_{0.037}O_2$(111) slab, we tested 4x4x1 and 3x3x1 k-points grids for sampling the Brillouin zone under the Monkhorst-Pack scheme [36], and found no significant difference in energy calculations. Thus, in this work, we used a 3x3x1 k-point sampling of the Brillouin zone for performing self-consistent calculations. The structural relaxations were accomplished according the Hellmann-Feynman approximation, while atomic positions were relaxed until the force acting on each atom was smaller than 0.02 eV/Å.

The standard DFT formulation usually fails to describe strongly correlated electrons, due to a deficient treatment of electron correlation. This limitation has been corrected to some extent by using the DFT+U method, where the introduction of a Hubbard parameter ‘U’ modified the electron self-interaction error and enhanced the description of the correlation effects [37,38]. Accordingly, we used the Hubbard parameters: U_{eff} = 5 eV for Ce(4f) states, and U_{eff} = 4.5 eV for Pr(4f) orbitals.

The value U_{eff} = 5 eV was chosen for the Ce(4f) states as it correctly described the atomic and electronic structure of both CeO_2 and CeO_{2-x} systems [30,39,40]. On the other hand, the value U_{eff} = 4.5 eV was considered reliable for describing the strong onsite

Coulomb repulsion among Pr(3d) electrons, as it has shown to reproduce the experimentally available data for PrO_2 such as lattice constant and band gap [41].

The resulting electronic structure of reduced ceria systems by using LDA+U or GGA+U, has been discussed in detail in the literature [42]. Castellani et al [43], pointed out that there is a clear indication that structural properties of CeO_2 such as lattice constant and bulk modulus are somewhat better represented by the LDA+U method; whereas both LDA+U and GGA+U results show a similarly good accuracy for Ce_2O_3. In a recent study, Kullgren reported the same result [44]. Nevertheless, for energy calculations of reduced CeO_{2-x}, Castellani et al [43] concluded that GGA+U approach provides a more accurate description than LDA+U does. Besides, in a recent review, Paier et al [45] compared quantum chemical studies of oxygen defects and surface chemistry of ceria and remarked that LDA suffers from unacceptably large errors for molecular binding energies and that drastic improvements are achieved with functionals based on GGA.

In the study of oxygen defects formation into the bulk crystal lattice of Ce-Pr mixed oxides, the GGA+U approach was also used by Tang et al [41] and Ahn et al [46]. Both works modeled the $Ce_{0.96875}Pr_{0.03125}O_2$ system, with 2 x 2 x 2 supercells, and used the PBE method. Also, for the Hubbard correction of Ce(4f) electrons, they considered values of U_{eff} = 4.5 eV [41], and 5.3 eV [46]. As mentioned before, a Hubbard parameter U_{eff} = 4.5 eV was also used for the Pr(4f) orbitals [41].

Therefore, our choice of the GGA(PBE)+U formalism is supported by all these previous studies and our own experience [47,12,13,48,49].

The selection of the Hubbard ‘U’ parameter deserves some additional attention. Castellani et al [43] and Paier et al [45], already mentioned that a key point is the choice of the ‘U’ value since it determines the final results to a large extent. In a very recent study, Nolan and Ganduglia-Pirovano [50] indicated that no single ‘U’ parameter can describe all material properties with the same degree of accuracy (see [50], and references therein).

For example, the case of CO adsorption on CeO_2(110) surface in Refs. [51,52], showed that U = 4.5 or 5 eV results in CO overbinding compared to experiment. With U = 2 eV, the adsorption energy is consistent with experiment, but this comes at the cost of not describing the electronic structure of the ceria surface accurately.

Finally, it is worthy to note that there are also questions regarding the specification of the atomic-like orbitals in DFT+U [53], the existence of multiple self-consistent solutions to the electronic structure [54–56], and the derivation of the “best” value for the ‘U’ parameter; which are still of great interest and debate.

Therefore, in this work we used Hubbard parameter values of U_{eff} = 5 eV for Ce(4f) states and U_{eff} = 4.5 eV for the Pr(4f) states as these values are considered to give reliable results.

3. RESULTS AND DISCUSSION

In this work, we studied the main characteristic of the 3.7 at% Pr-doped CeO_2(111) surface to clarify at fundamental level the effect of praseodymium on the surface chemistry of low-doped CeO_2-PrO_2 solid solutions. Starting from the stoichiometric $Ce_{0.963}Pr_{0.037}O_2$(111) surface, we computed the energy required to create an oxygen vacancy by considering different surface sites. After that, we investigated the oxygen replenishing process by computing O_2 molecule interactions. We also studied the reactivity of the formed active oxygen species by using CO as a testing molecule. For all the processes, we performed both energy calculations and electronic structure analysis. The electronic structure of optimized stoichiometric and O-deficient surfaces as well as that of optimized O_2/$Ce_{0.963}Pr_{0.037}O_2$(111) system was studied through density of states (DOS) and projected density of states (PDOS) concepts. Furthermore, oxidation state of Ce and Pr cations and electron occupancy of Ce(4f) and Pr(4f) states were computed by performing Bader charge and spin charge density analyses [57].

3.1 The stoichiometric $Ce_{0.963}Pr_{0.037}O_2$(111) surface

Our model of the $Ce_{0.963}Pr_{0.037}O_2$(111) surface exposes Ce and Pr cations together with surface and sub-surface O anions (see Fig. 1). Surface oxygen anions O1, O3 and O6 represent O–sites of different cationic environment. The oxygen O1 is located inside a triangle formed by Ce and Pr cations (Ce1, Ce3 and Pr). The O3 anion is located near Pr, but surrounded by Ce cations (Ce3, Ce4 and Ce5). Meanwhile, O6 is also in the center of a triangle formed by Ce cations (Ce2, Ce5 and Ce6) but located far away from Pr.

Figure 1

Concerning the electronic structure of the Pr-doped CeO_2(111) slab, Table 1 shows electron occupancy of (4f) states, Bader charge and spin magnetization for some selected cations. As regard of $Ce_{0.963}Pr_{0.037}O_2$(111), we computed electron occupancies for Ce(4f) and Pr(4f) states of 0 and 1.35, respectively. The Pr(4f) electron occupancy agrees with that of 1.44 calculated for the bulk structure of $Ce_{0.9688}Pr_{0.0312}O_2$ [41]. Note that our value

(1.35) is also consistent with those reported for Pr(4f) occupancy in PrO_2, between 1.5 and 1.6 [58–61]. Moreover, Bader charge calculations for Ce and Pr cations gave values of 9.6 e and 10.69 e, respectively; while computation of spin magnetization resulted in 0 μB for Ce cations, and 1.2 μB for Pr one.

Table 1

The total density of states (DOS) curve corresponding to the stoichiometric $Ce_{0.963}Pr_{0.037}O_2$(111) surface is shown in Fig. 2a. As well, the orbital projections of some selected ions (Pr, Ce3 and O1) are shown in Fig. 2b. Regarding the total DOS curve (see Fig. 3), the occupied valence band (VB) broadens between –4.25 eV and –0.25 eV. This band is mainly formed by O(2p) states and some contributions coming from Ce(4f) and Pr(4f) orbitals (see Fig. 2b). On the other hand, unoccupied Pr(4f) and Ce(4f) band runs from 0.5 eV to 2.5 eV. Note that empty Ce(4f) states localize around 2 eV. Meanwhile, there are localized peaks corresponding to Pr(4f) states both just above the Fermi level (at 0.5 eV) and in the range [1.0 eV – 2.5 eV] (see Fig. 2b). In this regard, the DOS analysis conducted in bulk structure of $Ce_{0.9688}Pr_{0.0312}O_2$ also revealed a new peak corresponding to metal-induced (Pr) gap states between the top of O(2p) valence-band and the bottom of Ce(4f) unoccupied-band [41].

Therefore, considering electron occupancy of Ce(4f) and Pr(4f) states, Bader charge and spin magnetization of Ce and Pr cations as well as density of states analysis, we estimated the oxidation states of Ce and Pr cations as Ce^{4+} and Pr^{4+}.

Figure 2, a & b

3.2 The $Ce_{0.963}Pr_{0.037}O_{2-x}$(111) surface with O-defects

The role of Pr dopant in the reducibility of CeO_2 has been evaluated through calculations of the energy required for creating an oxygen vacancy (ΔE_{O-Vac}) on the $Ce_{0.963}Pr_{0.037}O_2$(111) surface:

$$\Delta E_{O-Vac} = E[Ce_{0.963}Pr_{0.037}O_{2-x}(111)] + \tfrac{1}{2} E[O_2] - E[Ce_{0.963}Pr_{0.037}O_2(111)]$$

where: E[$Ce_{0.963}Pr_{0.037}O_{2-x}$(111)], E[$Ce_{0.963}Pr_{0.037}O_2$(111)], and E[$O_2$] are the energies of the relaxed surface slabs with and without surface O-vacancy, and the energy of the oxygen (O_2) molecule in vacuum, respectively.

With this, the calculated energy values for creation of the O1-, O3-, O4- and O6-defects are about 1 eV (see Table 2). These values agree with that reported for the $Ce_{0.9688}Pr_{0.0312}O_{1.9688}$ bulk structure [41]. This value is lower than that of 1.76 eV previously reported for surface O-defect formation in CeO_2(111) slab with p(4x4) expansion of the surface unit cell [62]. Thus, our results reveal that Pr doping significantly reduces the energy required for anionic defects formation on the CeO_2 surface despite the similar sizes of Ce and Pr cations. This indication agrees with the reported increase of oxygen vacancies concentration in Pr-doped CeO_2 solids [61,63,64].

The creation of a surface oxygen vacancy in the Pr-doped CeO_2(111) slab led to relaxations of many surface and subsurface ions. In the following, we describe the more representative ionic movements that resulted from formation of the O1 vacancy (an oxygen located near the Pr dopant).

Table 2

Table 3

Table 3 shows the distances from O1 oxygen and O1-hole to the most relaxed Ce1, Ce3 and Pr cations in $Ce_{0.963}Pr_{0.037}O_2$(111) and $Ce_{0.963}Pr_{0.037}O_{2-x}$(111) slabs, respectively. The final distance from Ce1 to the O1-hole is about 10% longer than the calculated length for Ce1–O1 bond in the Pr-substituted slab. Similarly, the distance from Ce3 and Pr to O1-hole is 7% larger than that corresponding to O1. For instance, Ce1, Ce3 and Pr cations moved 0.25 Å, 0.19 Å and 0.20 Å away from the O1-hole, respectively (see Fig. 3). The creation of O1 vacancy also modified the atomic position of many surface and inner–layer oxygen anions. Figure 3 also shows the main relaxations resulting in surface and subsurface anions; note the significant movement of a subsurface oxygen (0.27 Å) towards the O1-hole.

Figure 3

In addition, Table 1 shows Bader charge and spin magnetization for selected Ce cations as well as electron occupancy of their (4f) states. Electron population of Ce2 and Ce6 cations (~ 9.92) and spin magnetization of the corresponding Ce(4f) states (~1 μB), indicate that the two electrons left in the solid after removal of O1 were transferred to these ions. The reduction of two second-nearest-neighbor Ce cations to the oxygen vacancy agrees with reported results for big ceria supercell, indicating this configuration is most stable than that with two first-neighbor Ce^{3+} ions [65,66].

Concerning the electronic structure of $Ce_{0.963}Pr_{0.037}O_{2-x}$(111) slab, with a surface oxygen vacancy, Table 1 shows electron occupancy of (4f) states, Bader charge and spin magnetization for the reduced Ce and Pr cations. As it can be seen, the formation of O1-, O3-, O4- or O6-defect led to reduction of Pr and a Ce cation in Pr-doped CeO_2(111) slab. As well, Bader charge calculations show about 9.92 e for the corresponding reduced Ce cations (Ce3, Ce4, Ce8 and Ce6, respectively) and 10.96 e for Pr cation (see Table 1). These results point out that the two electrons left in the solid after formation of a surface O-defect were transferred to its neighbor Ce cation and to the Pr dopant. In addition, the corresponding Ce(4f) and Pr(4f) states show spin magnetizations of about 1 μB and 2 μB, respectively, reflecting the reduction of these Ce and Pr cations.

For instance, surface spin polarization of the $Ce_{0.963}Pr_{0.037}O_{2-x}$(111) slab with O1-defect (see Fig. 4a) shows positive magnetization of Ce3(4f) and Pr(4f) orbitals. Accordingly, the total DOS curve (see Fig. 4b) shows the formation of new peaks below the Fermi level; which are related to occupied Ce3(4f) states (at –0.5 eV) and Pr(4f) orbitals (at –1.2 eV) as exposed by the corresponding PDOS curves (see Fig. 4c). Therefore, we assigned a 3+ oxidation state to the reduced Ce3 and Pr cations. On the other hand, formation of O3-, O4- and O6-defect led to reduction of Ce4, Ce8 and Ce6 cations, respectively, as well as that of Pr dopant. Thus, oxidation state of these cations was attributed as $Ce^{3+}$and Pr^{3+}.

Figure 4, a–c

As previously discussed, our calculations consistently show the reduction of Pr dopant due to formation of a surface oxygen vacancy. This result agrees with the $Pr^{4+} \rightarrow Pr^{3+}$ transformation observed in the $Ce_{0.9688}Pr_{0.0312}O_{1.9688}$ bulk structure after creation of anionic defects [41]. Furthermore, our finding also agrees with experimental data reported for CeO_2 samples doped with Pr, obtained from XPS spectroscopy [67], and TPR, Raman

and EXAFS spectra [68], which show the existence of Pr^{4+}/Pr^{3+} redox couples in those solids.

3.3 Molecular oxygen adsorption on the O–defective $Ce_{0.963}Pr_{0.037}O_{2-x}$(111) surface

In this section, we report our results for calculations of oxygen interactions on the partially-reduced Pr-doped CeO_{2-x}(111) surface. We studied the configurations resulting from the O_2 molecule interaction above different anion vacancy sites (O1-, O3-, O4- and O6-hole) on the reduced $Ce_{0.963}Pr_{0.037}O_{2-x}$(111) surface. Moreover, to identify peroxide (O_2^-) and superoxide (O_2^{2-}) radical anions, we computed O–O bond length, vibration frequency, Bader charge and spin magnetization for the adsorbed dioxygen species and performed a PDOS analysis for the resulting O_2/CeO_2-based slabs.

The character and geometries of the activated oxygen species adsorbed near Pr cations may be different than on the undoped ceria surface. Therefore, for completeness, we also studied the interactions of molecular oxygen on the CeO_{2-x}(111) surface. We calculated the energy involved in O_2 adsorption ($\Delta E_{O2-Ads.}$) processes on the reduced CeO_{2-x}(111) and $Ce_{0.963}Pr_{0.037}O_{2-x}$(111) surfaces, as:

$$\Delta E_{O2-Ads} = E[O_2/slab] - E[O_2] - E[slab]$$

In this formula, $E[O_2/slab]$ is the computed total energy for O_2/CeO_{2-x}(111) or $O_2/Ce_{0.963}Pr_{0.037}O_{2-x}$(111); E[slab] is that for clean CeO_{2-x}(111) slab or $Ce_{0.963}Pr_{0.037}O_{2-x}$(111) one; finally, $E[O_2]$ is the corresponding total energy for an O_2 molecule in vacuum.

For both slabs, our calculations indicate that the interaction of one O_2 molecule on Ce cations located far away from an anionic vacancy is not favorable. Besides, there is almost no change in its bond length (1.25 Å) and vibration frequency (1424 cm^{-1}).

Focusing in the CeO_{2-x}(111) system, when the oxygen molecule was placed on top of Ce cations first-nearest-neighbors of an anionic defect, the O_2 species slid towards that defect. In this regard, we underline that similar configurations were obtained when the O_2 molecule was located over an O-hole. Thus, we only discussed the interaction of O_2 on O1 vacancy. Figure 5a, shows the structure obtained for this optimized O_2/CeO_{2-x}(111) system. Our results show that the dioxygen species adsorbed over the O1-hole tilted towards Ce cations, with a distance between the upper oxygen (O_U) and the lower one (O_L) of 1.45 Å. Thus, O_U bonded Ce3 ($d(O_U–Ce3)$ = 2.26 Å) while O_L bonded the surface

nearest-neighbor Ce cations. Although O_L almost occupies O1-hole, the new formed O_L–Ce bonds are longer than the original O1–Ce ones (see Table 4).

In this regard, we calculated an adsorption energy value of –1.49 eV for O_2 interaction on O1-hole (see Table 5). On the other hand, the spin magnetization of this species was computed in 0 μB (see Table 5). Moreover, Ce2 and Ce6 cations became reoxidized due to this interaction, suggesting that two electrons were transferred from the surface to the adsorbed dioxygen species. In this case, we computed a vibration frequency of 901 cm^{-1} for the adsorbed dioxygen species (see Table 5).

Figure 5, a & b

Table 4

Table 5

Experimentally, O_2 species adsorbed on ceria-based catalysts have been studied through Raman and IR spectra and identified as superoxide and peroxide radicals [69−76]. On this subject, it is worthy to note that the superoxide (O_2^-) radical has been associated with frequency values in the range [1050 cm^{-1} − 1150 cm^{-1}], while the peroxide (O_2^{2-}) one with those between 850 cm^{-1} and 950 cm^{-1}. Also, O−O bond length values of 1.43 Å and 1.34 Å have been considered as to distinguish between (O_2^{2-}) and (O_2^-) species [66]. Therefore, the main characteristics of adsorbed dioxygen species, calculated O−O distance of 1.45 Å and estimated oxidation state of 2^-, as well as the observed electron transference from reduced surface Ce cations to this species reveal its peroxide (O_2^{2-}) radical character.

Finally, we discuss the main characteristic of PDOS curves obtained for O_U(2p), O_L(2p), Ce3(4f), Ce2(4f) and Ce6(4f) states for the O_2/CeO_{2-x}(111) system with a dioxygen species adsorbed on O1-hole (see Fig. 5b). Self-evident, O_U(2p) and O_L(2p) states exhibit localized peaks around 0.5 eV below the top of the valence band. Moreover, at –0.5 eV there is a meaningful overlap of O_U(2p) and Ce3(4f) states revealing the chemical bonding between O_U and Ce3. Figure 5b, also reveals that projected curves of Ce2(4f) and Ce6(4f) states have localized peaks about 1.3 eV above the Fermi level. Thus, these curves reproduce well the essential description of Ce(4f) states attributed to Ce^{4+} cations, evidencing the reoxidation of Ce2 and Ce6 due to O_2 adsorption on the O1-hole.

Regarding molecular oxygen interactions on the $Ce_{0.963}Pr_{0.037}O_{2-x}$(111) surface, the calculations thoroughly show that the O_2 molecule set on top of Ce or Pr first-nearest-neighbor-cation of an anionic defect, slid towards that defect. Thus, we only present the results for O_2 interactions on surface oxygen vacancies. The adsorption energy values computed for O_2 interactions on different O-hole sites are shown in Table 5, while the corresponding structures can be seen in Fig. 6a–h.

Figure 6, a–h

In the case of O_2 interaction on O1-hole of $Ce_{0.963}Pr_{0.037}O_{2-x}$(111) surface, we calculated an adsorption energy value of –1.22 eV and O−O distance of 1.34 Å (see Table 5). The optimized structure of the resulting system, with the dioxygen species tilted to the surface, is shown in Fig. 6a. The lower oxygen (O_L) is barely sat on the O1-hole and bonded to its neighbor Ce and Pr cations. As it can be seen in Table 4, the new formed O_L–Cation bonds are longer than the original O1–Ce and O1–Pr ones as we computed distortions of about 14% and 19% for O_L–Pr and O_L–Ce1 lengths. Meanwhile, the upper oxygen (O_U) bent towards the surface and bonded Ce3 cation; the distance O_U–Ce3 distance was calculated in 2.51 Å. On the other hand, Bader analysis gave a charge value of 0.71 e. From this, we estimate an oxidation state of (–1.18). Moreover, Table 5 shows a spin polarization value of 0.99 μB for this species, indicating that only one electron was transferred from the surface to the adsorbed dioxygen species. The surface Ce3 cation became reoxidized due to this interaction (see Fig. 6b), suggesting that the dioxygen species adsorbed on the O1-hole is a superoxide radical. Furthermore, we computed its vibration frequency in 1137 cm^{-1} (see Table 5) which is consistent with those reported for adsorbed (O_2^-) species with values in the range [1050 cm^{-1} – 1150 cm^{-1}] [69–72,74,76].

As we mentioned before, because of the different cationic environment of surface anions we also studied the interactions of an oxygen molecule on O3-, O4- and O6-hole (see Table 5). Regarding O_2 interaction on O4-hole, that formed after removal of the oxygen located nearly close to Pr, Fig. 6c shows that O_U bent to the Pr dopant forming an O_U–Pr bond of 2.48 Å length. Noticeably, the new formed O_U–Pr bond is the longest one as it was elongated 32.77% compared to O4–Pr bond (see Table 4). Besides, the solid gave one electron to the adsorbed dioxygen species and only the Ce8 cation became reoxidized due to this interaction (see Fig. 6d). When the oxygen molecule was placed on O3-hole, it also tilted to the surface and O_U bonded Ce4 (see Fig. 6e). Again, the new

formed bonds are longer than the original O3–Ce ones (see Table 4), and the dioxygen species received one electron from Ce4 cation (see Fig. 6f). On the other hand, the results obtained from the interaction of molecular oxygen on O6-hole, which is far away from Pr dopant and surrounded only by Ce cations (Ce2, Ce5 and Ce6), present a rather different behavior. Figure 6g, shows the O_2 species adsorbed over the O6-hole ($\Delta E_{O2\text{-}Ads}$ = –1.20 eV) slightly inclined toward the surface, but, with no bonds creation between O_U and Ce cations. Meanwhile, Table 5 reports spin polarization value of –0.97 μB for this species and vibration frequency of 1126 cm^{-1} for the adsorbed dioxygen species; which suggest the formation of (O_2^-) radical (see Fig. 6h).

"Related to oxygen molecule interactions on surface anion vacancies, it is worthy to note that both singly occupied and unoccupied molecular orbitals of O_2 triplet ground state are <pi>(2p)* states [77,78]. Besides, reduced surface Ce^{3+} cations might donate its localized (4f) electrons to an adsorbed species. Thus, interaction of O_2 molecule on the O-holes of ceria-based catalysts could cause some electron density transference from reduced surface cations to the unoccupied π(2p)* orbitals of adsorbed O_2, leading to formation of negatively charged dioxygen radicals. In this respect, our results show that the O-deficient CeO_{2-x}(111) surface became reoxidized after O_2 interaction on O1-hole. Indeed, the solid donated the (4f) electrons of two Ce^{3+} anions to the adsorbed dioxygen species leading to formation of a peroxide (O_2^{2-}) radical. Furthermore, spin density calculations show that there are no spin electrons for (O_2^{2-}) radical and, thus, indicate that the peroxide species adsorbed on this surface are diamagnetic.

Different from this, we found out the $Ce_{0.963}Pr_{0.037}O_{2-x}$(111) surface remains partially reduced after O_2 interaction on O1-, O3-, O4- or O6-hole. As previously reported in a recent theoretical-experimental work [9], Pr cations like better to remain as Pr^{3+} while Ce^{3+} ions tend to reoxidize ($Ce^{3+} \rightarrow Ce^{4+}$). Then, the O-deficient Pr-doped surface would transfer less electron density to adsorbates than the undoped one. In fact, only the (4f) electron of Ce^{3+} anion was donated from the substrate to unoccupied π(2p)* orbitals of the adsorbed dioxygen species. In this regard, the transfer of one electron from the ceria surface to the adsorbed O_2 was taken as a key criterion for concluding the formation of (O_2^-) species [66]. Therefore, our charge transference calculations support the idea that Pr dopant promotes formation of most reactive superoxide radicals (O_2^-). Correspondingly, the calculated O_2 adsorption energy on the Pr-doped ceria surface is lower than on the undoped case.

Concerning the vibration frequency of dioxygen species adsorbed on O3-, O4- and O6-hole, we calculated intensity values in the range [1131 cm^{-1} – 1126 cm^{-1}] (see Table 5); which agree with those of 1050 cm^{-1} – 1150 cm^{-1} assigned to (O_2^-) species [69–72,74,76]. Moreover, peaks of 1126 cm^{-1} – 1135 cm^{-1} have been attributed to superoxide-like species [79]. Particularly, a frequency value of 1128 cm^{-1} has been reported for these species and suggested that surface defects play a significant role in generation of superoxide-like radicals [75]. Recently, it was also demonstrated that surface morphology is an important factor for observation of adsorbed oxygen species [80]. Therefore, our calculated frequency values convincingly confirm the formation of (O_2^-) species on the O-hole sites of $Ce_{0.963}Pr_{0.037}O_{2-x}$(111) surface; revealing again that low Pr doping strongly promotes the adsorption of superoxide radicals.

Overall, we found out that molecular oxygen interactions on $Ce_{0.963}Pr_{0.037}O_{2-x}$(111) surface results in side-on superoxide (O_2^-) species, which are up to 0.29 eV less stable than the peroxide (O_2^{2-}) formed on clean CeO_{2-x}(111); indicating that Pr doping would promote the existence of more activated oxygen radicals.

Finally, we discuss the electronic structure computed for two selected $O_2/Ce_{0.963}Pr_{0.037}O_{2-x}$(111) systems by using the concept of projected density of states on significant O(2p), Ce(4f) and Pr(4f) orbitals. In this respect, Fig. 7a presents PDOS curves corresponding to O_U(2p), O_L(2p), Ce8(4f) and Pr(4f) states for the $O_2/Ce_{0.963}Pr_{0.037}O_{2-x}$(111) system with a dioxygen species adsorbed on O4-hole. Below the Fermi level, we can see that O_U(2p) and O_L(2p) states shear electron density from –2.0 eV to –1.0 eV. In the energy range between –2.0 eV and –0.5 eV, there is an important overlap between O_L(2p) and Pr(4f) states. In addition, O_L(2p) orbitals also overlap with Ce8(4f) states from –2.0 eV to –1.0 eV. These bands essentially reflect the formation of long O_L–Pr (3.12 Å) and O_L–Ce8 (2.58 Å) bonds. Meanwhile, O_U(2p) and Pr(4f) orbitals shear electron density from –2.0 eV to –1eV in agreement with creation of O_U–Pr bond. Furthermore, the PDOS curve of Pr(4f) states shows the binding sharp peak placed 0.5 eV closer to Fermi level when compared with that of Pr^{3+} in the clean surface. This fact perfectly agrees with formation of the O_U–Pr bond (2.48 Å). On the other hand, at 1.5 eV above the Fermi level we can see the localized Ce8(4f) peak; which reveals the reoxidation of Ce8 ($Ce^{3+} \rightarrow Ce^{4+}$) by the transference of one electron to adsorbed dioxygen species.

Figure 7b, presents PDOS curves corresponding to projections of O_U(2p), O_L(2p), Ce6(4f) and Pr(4f) states, for the $O_2/Ce_{0.963}Pr_{0.037}O_{2-x}$(111) system with a dioxygen species adsorbed on O6-hole. Looking at the binding energy zone, we realize that O_U(2p) and

O_L(2p) states shear electron density just below the Fermi level and around –5.0 eV. The PDOS curve of Pr(4f) states shows the sharp peak placed just below the Fermi, indicating no donation of electrons from Pr to adsorbed dioxygen species. Above the Fermi level, Ce6(4f) states contributions mainly come from the localized peak at 1.5 eV; reflecting the reoxidation of Ce6 cation ($Ce^{3+} \rightarrow Ce^{4+}$) after transference of one electron to adsorbed dioxygen species. Interestingly, there are also empty O_U(2p) and O_L(2p) states just above the Fermi level; which suggest a high reactivity of the superoxide (O_2^-) radical adsorbed on O6-hole.

Figure 7, a & b

3.4 CO adsorption on the $Ce_{0.963}Pr_{0.037}O_2$(111) surface

Our calculations show that replenishment of anionic vacancies with molecular oxygen leads to formation of superoxide (O_2^-) species on the $Ce_{0.963}Pr_{0.037}O_{2-x}$(111) surface. This result indicates that Pr doping would promote the reactivity of ceria surface not only by enhancing oxygen donation but also facilitating the formation of highly active oxygen species. Thus, to understand the catalytic properties of this surface, we used CO as a probe molecule and investigated its reaction with adsorbed (O_2^-) superoxide radicals. For completeness, we also evaluated CO interactions on the undoped O_2/CeO_{2-x}(111) system.

The CO adsorption energy ($\Delta E_{CO-Ads.}$) on the $O_2/Ce_{0.963}Pr_{0.037}O_{2-x}$(111) system was calculated as:

$$\Delta E_{CO-Ads} = E[CO/slab] - E[CO] - E[slab]$$

Where, E[CO/slab] is the computed total energy for the CO interaction on the $O_2/Ce_{0.963}Pr_{0.037}O_{2-x}$(111) system; E[slab] is that for the $O_2/Ce_{0.963}Pr_{0.037}O_{2-x}$(111) system and E[CO] corresponds to the total energy of a CO molecule in vacuum.

With this formula, we computed CO interactions on two different $O_2/Ce_{0.963}Pr_{0.037}O_{2-x}$(111) systems; which have (O_2^-) superoxide species adsorbed on the O–hole left by O4 or O6 oxygen donation.

For completeness, we also computed CO molecule interaction on the undoped O_2/CeO_{2-x}(111) system. Our calculations indicate that CO interaction on peroxide (O_2^{2-}) species adsorbed on the CeO_{2-x}(111) surface led to formation of a CO_2 molecule, which

would be easily released to gas phase as suggested by its very low adsorption energy ($\Delta E_{CO2\text{-}Ads}$ = –0.1 eV). As regard of pure CeO_2, it is commonly accepted that CO adsorption on the clean (111) surface is very weak [81].

Concerning $O_2/Ce_{0.963}Pr_{0.037}O_{2-x}$(111) systems, CO interaction with (O_2^-) superoxide species adsorbed on O6-hole led to formation of a CO_2 molecule floating on the surface. For this interaction, we calculated a CO_2 adsorption energy value of –0.21 eV. The optimized configuration (see Fig. 8a) exhibit the conventional O–C–O geometry with an O–C–O angle of 179°, and C–O bonds length of 1.17 Å and 1.18 Å which compare well with the 1.18 Å in the gas phase. Besides, the computed vibration frequency value of 2375 cm^{-1} agrees with that of 2381 cm^{-1} reported for the asymmetric vibrational mode of a free CO_2 molecule. Meanwhile, Bader charge calculations gave 16 electrons for that formed species. All these values, very close to those of a free CO_2 molecule: C–O bonds length of 1.20 Å, O–C–O angle of 180° and total Bader charge of 16 e, indicate the formation of a neutral floating CO_2 molecule. Bader analysis also indicates that Ce and Pr cations are in 4+ oxidation state (9.64 e and 10.75 e for Ce8 and Pr, respectively) in the remaining stoichiometric surface (see Fig. 8a). Altogether, the results show that CO interactions on (O_2^-) radicals adsorbed on the O–deficient $Ce_{0.963}Pr_{0.037}O_{2-x}$(111) surface led to formation of a floating CO_2 molecule; which would act as an intermediate for the full oxidation reaction:

$$CO + O_2/Ce_{0.963}Pr_{0.037}O_{2-x}(111) \rightarrow CO_{2(gas\ phase)} + Ce_{0.963}Pr_{0.037}O_2(111)$$

Figure 8, a–c

The CO molecule can also react with the (O_2^-) radical adsorbed on the O4-hole of $Ce_{0.963}Pr_{0.037}O_{2-x}$(111) surface, by interacting with O_U anion or O_U–O_L bridge (O_U and O_L indicate upper and lower oxygen species of dioxygen radical, respectively). The interaction of CO molecule with O_U anion also led to formation of floating CO_2 molecule ($\Delta E_{CO2\text{-}Ads}$ = –0.22 eV).

On the other hand, CO interaction on O_U–O_L bridge of (O_2^-) radicals adsorbed on the O4–hole of $Ce_{0.963}Pr_{0.037}O_{2-x}$(111) surface was more exothermic and a bent CO_2 species was formed (see Fig. 8b). For this configuration, we calculated a CO_2 adsorption energy value of –0.73 eV. This value reflects bonding interactions between C and both O_U and O_L species. As it can be seen in Fig. 8b, the resulting bent OC–O_U group has C–O

bonds of 1.26 Å and 1.28 Å long and a O–C–O_U angle of 124°. However, this group also bonded O_L anion (d(C–O_L = 1.34 Å), pulling it outward the surface and preventing the fulfilling of O4-hole. Besides, Bader charge analysis indicates a total of 23.2 e for the whole "CO_3" species as well as 9.60 e and 10.75 e for Ce6 and Pr cations, respectively. Thus, these cations are in 4^+ oxidation state in the remaining non-stoichiometric surface (see Fig. 8b). Additionally, for the (CO_3) species we calculated a vibration frequency of 1436 cm^{-1}; which is in good agreement with reported bands in the region of 1460 cm^{-1} – 1510 cm^{-1} assigned by different groups to "monodentate" carbonate [82]. All these calculations indicate the formation of a carbonate anion (CO_3^{2-}) after CO adsorption.

The previous results allow us to postulate that O_2/$Ce_{0.963}Pr_{0.037}O_{2-x}$(111) system with an ($O_2^-$) species adsorbed on the O-hole adjacent to Pr dopant can transfer electron density to CO molecule. In this regard, we present a charge distribution plot for the adsorption zone. The charge density difference ($\Delta\rho$), was obtained as:

$$\Delta\rho = \rho_{CO/System} - \rho_{CO} - \rho_{System},$$

where $\rho_{CO/System}$ represents the charge density of the configuration computed for CO interaction on O_U–O_L bridge; while ρ_{System} and ρ_{CO} refers to charge density of distorted O_2/$Ce_{0.963}Pr_{0.037}O_{2-x}$(111) system and CO, respectively.

Figure 8c, shows a plot for the charge distribution at the adsorption zone. The region of charge accumulation (isovalue +0.003) is presented in yellow color and that of electron depletion (isovalue –0.003) in blue color. As we can see, there is a significant increase of electron density in the region corresponding to CO_2–O_L group. A strong charge accumulation is found just on the oxygen anions bonded to carbon. Meanwhile, a depletion of electron density appears on the lower side of the carbonate-type species facing the Pr dopant ($Pr^{3+} \rightarrow Pr^{4+}$ reoxidation) as well as on the surface of ceria substrate.

Regarding ceria, it is worth noting that CO adsorption was found to result (beyond physisorption) in its oxidation and formation of carbonates on the more reactive (110) and (100) surfaces of CeO_2, where the C atom is bound to one or two surface O centers, respectively [81]. Different CO vibrational frequencies have been reported for the adsorbed carbonates, depending on the CeO_2 surface [81]: 1710 cm^{-1}, 1108 cm^{-1} and 1271 cm^{-1} for the (CO_3) group formed on the (110) surface, and 1758 cm^{-1}, 708 cm^{-1} and 1117 cm^{-1} for the (CO_3) group formed on the (100) one. Besides, surface carbonate species formed on ceria surfaces have also been characterized by several authors through infrared (IR)

spectroscopy. Recently, evaluation of thermal stability of the IR signals in TPD spectra has allow to assign the band at 1396 cm^{-1} to a surface carbonate (CO_3) species [83].

Therefore, we underline that only the superoxide (O_2^-) species closest to Pr dopant has shown the ability to adsorb the CO molecule forming a bent CO_2 species. So, this finding suggests a net influence of the (O_2^-)–Pr^{3+} interphase interaction in the process of developing carbonate-type species through a redox interaction in the Pr-doped CeO_{2-x}(111) surface. In this regard, the buildup of stable carbonate species could be correlated with deactivation of those highly reactive surface radicals linked to reduced praseodymium (Pr^{3+}) dopant. Thus, it is worth mentioning that experimental studies of CO adsorption on nanostructured praseodymium oxide have indicated that oxidation of this molecule involves its adsorption as a bidentate carbonate, which then transforms into a monodentate carbonate and desorbs as CO_2 [84].

In summary, our DFT+U calculations indicate that CO molecule can react with (O_2^-) radicals adsorbed on reduced $Ce_{0.963}Pr_{0.037}O_{2-x}$(111) surface leading to formation of: (i) floating CO_2 molecule + stoichiometric $Ce_{0.963}Pr_{0.037}O_2$(111) surface, or (ii) carbonate-type (CO_3^{2-}) species directly adsorbed on the O–hole near Pr dopant + nonstoichiometric $Ce_{0.963}Pr_{0.037}O_{2-x}$(111) surface

CONCLUSIONS

In this work, we performed DFT+U calculations to study the redox behavior of low Pr-doped CeO_2(111) surface. The addition of Pr leads to formation of metal-induced Pr gap states (just above the Fermi level), which can receive electron density. Indeed, our results show that Pr dopant strongly facilitates surface oxygen donation, with the consequential formation of Pr^{4+}/Pr^{3+} and Ce^{4+}/Ce^{3+} redox couples. Concerning the interactions of O_2 molecule on the $Ce_{0.963}Pr_{0.037}O_{2-x}$(111) surface, the results indicate preferential adsorption of dioxygen species on the O-hole located near a Ce^{3+} cation; which adopts a Ce^{4+} state, while the reduced Pr cation remains as Pr^{3+}. The calculations show that Pr promotes the adsorption of superoxide (O_2^-) radicals on Pr-doped CeO_2(111) surface. The formation of (O_2^-) species is strongly related to electron density transfer from reduced surface Ce^{3+} cation to π(2p)* molecular orbital of the adsorbed dioxygen species. We also studied the reactivity of adsorbed (O_2^-) species by computing CO interactions on these radicals. The CO molecule can easily react with (O_2^-) radicals leading to floating CO_2 species. Additionally, this molecule can also interact on the (O_2^-)/Pr^{3+} interphase and forms weakly adsorbed carbonate-type intermediates.

ACKNOWLEDGMENTS

The authors acknowledge to the University of Buenos Aires (UBA), ANPCyT and CONICET for their financial support.

REFERENCES

[1. A. Trovarelli. *Catal. Rev. Sci. Eng.* 38 (1996) 439–520.

[2] Z. Yang , T.K. Woo, K. Hermansson. *J. Chem. Phys.* 124 (2006) 224704 (7 pp.)

[3] D. Widmann, R. Leppelt, R.J. Behm. *J. Catal.* 251 (2007) 437–442.

[4] T. Masui, N. Imanaka. *Mater. Integr.* 16 (2003) 16–29.

[5] Y. Zongxian, F. Zhaoming, W. Yanwei, L. Zhansheng. *J. Phys. Chem. C* 112 (2008) 15341–15347.

[6] N. V. Skorodumova, M. Baudin, K. Hermansson. *Phys. Rev. B: Condens. Matter Mater. Phys.* 69 (2004) 075401 (8 pp.).

[7] Y. Tang, H. Zhang, L. Cui, C. Ouyang, S. Shi, W. Tang, H. Li, J. Lee, L. Chen. *Phys. Rev. B* 82 (2010) 125104 (9 pp.).

[8] E. Poggio-Fraccari, F. Mariño, M. Laborde, G. Baronetti. *Appl Catal A: Gen.* 460 (2013) 15–20.

[9] E. Poggio-Fraccari, B. Irigoyen, G. Baronetti, F. Mariño . *Appl. Catal. A: Gen.* 485 (2014) 123–132.

[10] D.A. Andersson, S.I. Simak, N.V. Skorodumova, I.A. Abrikosov, B. Johansson, *Appl. Phys. Lett.* 90 (2007) 031909 (3 pp.).

[11] T. Yuanhao, Z. Hua, C. Lixia, O. Chuying, S. Siqi, T. Weihua, L. Hong, L. Jong-Sook, C. Liquan, *Phys. Rev. B* 82 (2010) 125104 (9 pp.).

[12] D. García Pintos, A. Juan, B. Irigoyen, *Intern. J. Hydrogen Energy* 37 (2012) 14937–14944.

[13] D. García Pintos, A. Juan, B. Irigoyen, *J. Phys. Chem. C* 117 (35) (2013) 18063–18073.

[14] A. Gupta, U.V. Waghmare, M.S. Hegde, *Chem. Mater.* 22 (2010) 5184–5198.

[15] P. Dholabhai, J. Adams, P. Crozier, R. Sharma, *Chem. Phys.* 132 (2010) 094104 (9 pp.).

[16] K. Ahn, D. Su Yoo, D. Hari Prasad, H.-W. Lee, Y.-C. Chung, J.-H. Lee, *Chem. Mater.* 24 (2012) 4261−4267.

[17] Y. Madier, C. Descorme, A.M. Le Govic, D.J. Duprez, *Phys. Chem. B* 103 (1999) 10999–11006.

[18] Y. Choi, H. Abernathy, H.-T. Chen, M. Lin, M. Liu, *ChemPhysChem* 7 (2006) 1957–1963.

[19] M. Nolan, *J. Chem. Phys.* 130 (2009) 144702 (10 pp.).

[20] C. Wanglai, L. Yue, W. Zhongbiao, W. Haiqiang, W. Xiaole, *Phys. Chem. Chem. Phys.* 14 (2012) 5769–5777.

[21] G. Xiao, S. Li, H. Li, L. Chen, *Microporous Mesoporous Mater.* 120 (2009) 426–431.

[22] R. D. Shannon, *Acta Crystallogr. Sect. A* 32 (1976) 751–767.

[23] M. Luo, Z. Yan, L. Jin, J. Molec. Cat. A: Chem. 260 (2006) 157–162.

[24] B. Reddy, G. Thrimurthulu, L. Katta, J. Phys. Chem. C 113 (2009) 15882–15890.

[25] Z. Song, W. Liu, H. Nishiguchi, A. Takami, K. Nagaoka, Y. Takita, Appl Catal. A: Gen. 329 (2007) 86–92.

[26] D. Kim, J. Am. Ceram. Soc. 72 (1989) 1415–1421.

[27] S. Tsunekawa, R. Sivamohan, S. Ito, A. Kasuya, T. Fukuda, Nanos. Mater. 11 (1999) 141–147.

[28] L. Eyring. *Handbook on the physics and chemistry of rare earths*. North–Holland, Amsterdam: K.A. Gschneider and L. Eyring (Eds.) 1979.

[29] J.C. Conesa, *Surf. Sci.* 339 (1995) 337–352.

[30] M. Nolan, S. Grigoleit, D.C. Sayle, S.C. Parker, G.W. Watson, *Surf. Sci.* 576 (2005) 217–229.

[31] N.V. Skorodumova, M. Baudin, K. Hermansson, *Phys. Rev. B* 69 (2004) 075401 (8pp).

[32] G. Kresse, J. Furthmuller, *Comput. Mater. Sci.* 6 (1996) 15–50.

[33] G. Kresse, J. Hafner, *Phys. Rev. B* 47 (1993) 558–561.

[34] G. Kresse, D. Joubert, *Phys. Rev. B* 59 (1999) 1758–1775.

[35] J. Perdew, K. Burke, M. Ernzerhof, *Phys. Rev. Lett.* 77 (1996) 3865–3868.

[36] H. Monkhorst, J. Pack, *Phys. Rev. B* 13 (1976) 5188–5192.

[37] S. Dudarev, G. Botton, S. Savrasov, C. Humphreys, A. Sutton, *Phys. Rev. B* 57 (1998) 1505–1509.

[38] V. Anisimov, J. Zaanen, O. Andersen, *Phys. Rev. B* 44 (1991) 943–954.

[39] H. Li, H. Wang, X. Gong, Y. Guo, Y. Guo, G. Lu, P. Hu, *Phys. Rev. B* 79 (2009) 193401(1–4).

[40] C. Castleton, J. Kullgren, K. Hermansson, *J. Chem. Phys.* 127 (2007) 244704(1–11).

[41] Y. Tang, H. Zhang, L. Cui, C. Ouyang, S. Shi, W. Tang, H. Li, J. Lee, L. Chen, Phys. Rev. B 82 (2010) 125104(1–9).

[42] M. V. Ganduglia-Pirovano, A. Hofmann, J. Sauer, Surf. Sci. Rep. 62 (2007) 219–270.

[43] N. J. Castellani, M. M. Branda, K. M. Neyman, F. Illas, J. Phys. Chem. C 113 (2009) 4948–4954.

[44] J. Kullgren, Oxygen Vacancy Chemistry in Ceria, PhD Thesis (University of Uppsala), https://www.diva-portal.org/smash/get/diva2:491677/FULLTEXT01.pdf, 2012.

[45] J. Paier, C. Penschke, J. Sauer, *Chem. Rev.*, 113 (2013) 3949–3985.

[46] K. Ahn, D. Su Yoo, D. Hari Prasad, H.–W. Lee, Y.–Ch. Chung, J.–H. Lee, *Chem. Mater.* 24 (2012) 4261–4267.

[47] F. Cova, D. García Pintos, A. Juan, B. Irigoyen, J. Phys. Chem. C 115 (2011) 7456–7465.

[48] D. García Pintos, A. Juan, B. Irigoyen, Appl. Surf. Sci. 313 (2014) 784–793.

[49] O. D'Alessandro, D. García Pintos, A. Juan, B. Irigoyen, J. Sambeth, Appl. Surf. Sci. 359 (2015) 14–20.

[50] M. Nolan, M.V. Ganduglia-Pirovano, Appl. Catal. B: Environ. 197 (2016) 313–323.

[51] M. Huang, S. Fabris, J. Phys. Chem. C 112 (2008) 8643.

[52] M. Nolan, Catalysis by Materials with Well-Defined Structures, in: Z. Wu, S.H. Overbury (Eds.), Elsevier, 2015, pp. 159.

[53] S. Fabris, G. Vicario, G. Balducci, S. de Gironcoli, S. Baroni, J. Phys. Chem. B 109 (2005) 22860–22867.

[54] B. Meredig, A. Thompson, H.A. Hansen, C. Wolverton, A. van de Walle, Phys.Rev. B 82 (2010) 195128 (1–5).

[55] B. Dorado, M. Freyss, B. Amadon, M. Bertolus, G. Jomard, P. Garcia, J. Phys.: Condens. Matter 25 (2013) 333201 (1–13).

[56] J.P. Allen, G.W. Watson, Phys. Chem. Chem. Phys. 16 (2014) 21016–21031.

[57] G. Henkelman, A. Arnaldsson, H. Jónsson, *Comput. Mater. Sci.* 36 (2006) 354–360.

[58] A. Bianconi, A. Kotani, K. Okada, R. Giorgi, A. Gargano, A. Marcelli, T. Miyahara, *Phys. Rev. B* 38 (1988) 3433 (5 pp.).

[59] H. Ogasawara, A. Kotani, K. Okada, B. T. Thole, *Phys. Rev. B* 43 (1991) 854−859.

[60] S. M. Butorin, L. C. Duda, J. H. Guo, N. Wassdahl, J. Nordgren, M. Nakazawa, A. Kotani, *J. Phys.: Condens. Matter.* 9 (1997) 8155−8160.

[61] A. Hartridge, M. G. Krishna, A. K. Bhattacharya, *Mater. Sci. Eng. B* 57 (1999) 173−178.

[62] J. Paier, C. Penschke, J. Sauer, *Chem. Rev*. 113 (2013) 3949–3985.

[63] N.V. Skorodumova, S.I. Simak, B.I. Lundqvist, I.A. Abrikosov, B. Johansson, *Phys. Rev. Lett.* 89 (2002) 166601 (4 pp.).

[64] Z.–Y. Pu, J.–Q. Lu, M.–F. Luo, Y.–L. Xie, *J. Phys. Chem. C* 111 (2007) 18695−18702.

[65] M. V Ganduglia-Pirovano, J. L. F. Da Silva, J. Sauer, *Phys. Rev. Lett.* 2009, 102 (2), 026101 (4 pp.).

[66] Y. Zhao, B.-T. Teng, X.-D. Wen, Y. Zhao, Q.-P. Chen, L.-H. Zhao, M.-F. Luo, *J. Phys. Chem. C* 116 (2012) 15986−15991.

[67] G. Xiao, S. Li, H. Li, L. Chen, *Microporous Mesoporous Mater.* 120 (2009) 426−431.

[68] K. Ahn, D. Yoo, D. Hari Prasad, Y.–Ch. Chung, J.–H. Lee, *Chem. Mater.* 24 (2012) 4261−4267.

[69] J. Kaspar, P. Fornasiero, M. Graziani, *Catal. Today* 50 (1999) 285−298.

[70] K. Azzam, I. Babich, K. Seshan, L. Lefferts, *J. Catal.* 251 (2007) 153−162.

[71] T. H. Etsell, S. N. Flengas, *Chem. Rev.* 70 (1970) 339−376.

[72] J. Soria, A. Martinez-Arias, J.C. Conesa, *Faraday Trans.* 91 (1995), 1669−1678.

[73] C. Li, K. Domen, K.-I. Maruya, T. Onishi, *J. Catal.* 123 (1990) 436−442.

[74] V. Pushkarev, V. Kovalchuk, J. d'Itri, *J. Phys. Chem. B* 108 (2004) 5341−5348.

[75] C. Li, K. Domen, K. Maruya, T.Onishi, *J. Am. Chem. Soc.* 111 (1989) 7683−7687.

[76] C. Binet, M. Daturi, J.-C. Lavalley, *Catal. Today* 50 (1990) 207−234.

[77] Mark K. Winter, Chemical Bonding, in: Oxford University Press, Oxford, 1994, p. 46.

[78] Geoff Rayner-Canham and Tina Overton, Descriptive Inorganic Chemistry, in: W.H. Freeman and Company (Eds.), New York, 2010, pp. 414–415.

[79] Y. Choi, H. Abernathy, H.-T. Chen, M. Lin, M. Liu, X. Lu, P. Faguy, *ChemPhysChem* 7 (2006) 1957–1963.

[80] Y. Zhang, Z. Kang, J. Dong, H. Abernathy, M. Liu, *J. Solid State Chem.* 179 (2006) 1733−1738.

[81] M. Nolan, S.C. Parker, G.W. Watson, *Surf. Sci.* 600 (2006) L175–L178.

[82] G.N. Vayssilov, M. Mihaylov, P. St. Petkov, K.I. Hadjiivanov, K.M. Neyman, *J. Phys. Chem. C* 115 (2011) 23435–23454.

[83] G. Finos, S. Collins, G. Blanco, E. del Rio, J. Cíes, S. Bernal, A. Bonivardi, *Catal.*

Today 180 (2012) 9-18.

[84] Y. Borchert, P. Sonström, M. Wilhelm, H. Borchert, M. Bäumer, *J. Phys. Chem. C* 112 (2008) 3054–3063.

CAPTIONS FOR FIGURES

Figure 1. Front view of the $Ce_{0.963}Pr_{0.037}O_2(111)$ surface model. Note that some surface anions have different cationic environment: O1 is surrounded by Ce and Pr cations, O3 is near Pr and surrounded by Ce cations, while O6 is far away from Pr and neighboring Ce cations. Color coding of spheres used for ions representation throughout the paper: cerium (Ce) in cyan, oxygen (O) in red and praseodymium (Pr) in ochre.

Figure 2. Density of States (DOS) of stoichiometric $Ce_{0.963}Pr_{0.037}O_2(111)$ slab. (a) Total DOS curve (spin-up). (b) Projected DOS (PDOS) curves for Pr(4f), Ce3(4f) and O1(2p) orbitals (spin-up). Energy values are relative to Fermi level. The peak corresponding to metal-induced (Pr) gap states is shown above the Fermi level.

Figure 3. $Ce_{0.963}Pr_{0.037}O_{2-x}(111)$ slab: front view of the most significant ion relaxations resulting from removal of surface oxygen O1. The empty circle shows the location of the oxygen vacancy.

Figure 4. Electronic structure of the $Ce_{0.963}Pr_{0.037}O_{2-x}(111)$ slab with O1-defect. (a) Spin polarization at a 0.05 e $Å^{-3}$ isovalue for Ce3(4f) and Pr(4f) orbitals. Positive and negative values are indicated in yellow and gray, respectively. (b) DOS curve (spin-up). (c) PDOS curves (spin-up) for Ce3(4f) and Pr(4f) orbitals. O1-defect is represented by an empty circle. Energy values are relative to Fermi level.

Figure 5. The $O_2/CeO_{2-x}(111)$ system with a dioxygen species adsorbed on O1-hole. (a) Side view of the optimized structure. (b) Projected Density of States (PDOS) curves of $O_U(2p)$, $O_L(2p)$, Ce2(4f) and Ce6(4f) orbitals. Energy values are relative to Fermi level.

Figure 6. The $O_2/Ce_{0.963}Pr_{0.037}O_{2-x}(111)$ systems. (a) Side view of O_2 adsorbed on O1-hole. (b) Spin polarization surface resulting from O_2 adsorption on O1-hole. (c) Side view of O_2 adsorbed on O4-hole. (d) Spin polarization surface resulting from O_2 adsorption on O4-hole. (e) Side view of O_2 adsorbed on O3-hole. (f) Spin polarization surface resulting from O_2 adsorption on O3-hole. (g) Side view of O_2 adsorbed on O6-hole. (h) Spin polarization surface resulting from O_2 adsorption on O6-hole. Note that all surfaces were drawn at a 0.05 e $Å^{-3}$ isovalue. Positive and negative values are indicated in yellow and gray, respectively. The O_2 interaction on the surface O-hole resulted in formation of a superoxide radical by the transference of one electron from a reduced Ce cation.

Figure 7. Projected Density of States (PDOS) curves of $O_U(2p)$, $O_L(2p)$, Ce(4f) and Pr(4f) orbitals for selected $O_2/Ce_{0.963}Pr_{0.037}O_{2-x}(111)$ systems. (a) O_2 adsorbed on O6-hole. (b) O_2 adsorbed on O4-hole. Energy values are relative to Fermi level.

Figure 8. CO adsorption on the $O_2/Ce_{0.963}Pr_{0.037}O_{2-x}$(111) system. (a) CO_2 molecule floating on the surface formed from CO interaction with dioxygen radical (O_2^-) adsorbed on O6-hole. (b) Carbonate-type (CO_3^{2-}) anion formed after CO interaction on the O–O bridge of dioxygen radical (O_2^-) adsorbed on O4-hole. (c) Charge density difference graph for CO interaction on the O–O bridge of dioxygen radical (O_2^-) adsorbed on O4-hole. The region of charge accumulation (isovalue +0.003) is presented in yellow color, and that of electron depletion (isovalue –0.003) in blue color.

Table 1. Electron occupancy of (4f) states, Bader charge, and spin magnetization for selected cations on undoped and Pr-doped CeO_2(111) slabs

Slab	Vacancy	Cation	Electron Occupancy (4f) states	Bader Charge (e)	Spin Magnetization (μB)	Estimated Oxidation States
CeO_{2-x}(111)	O1	Ce2	0.97	9.85	0.99	3+
		Ce6	0.97	9.86	0.99	3+
CeO_2(111)		Ce2	0	9.60	0	4+
		Ce6	0	9.60	0	4+
$Ce_{0.963}Pr_{0.037}O_{2-x}$(111)	O1	Ce3	0.96	9.92	1.00	3+
		Pr	1.97	10.96	2.02	3+
	O3	Ce4	0.93	9.92	0.98	3+
		Pr	1.97	10.90	2.01	3+
	O4	Ce8	– 0.96*	9.93	– 0.93*	3+
		Pr	1.96	10.96	1.99	3+
	O6	Ce6	0.96	9.94	1.00	3+
		Pr	1.97	10.89	2.01	3+
$Ce_{0.963}Pr_{0.037}O_2$(111)		Ce3	0	9.60	0	4+
		Ce4	0	9.61	0	4+
		Ce6	0	9.60	0	4+
		Ce8	0	9.60	0	4+
		Pr	1.35	10.70	1.23	4+

* spin down

Table 2. Oxygen vacancy formation energy ($\Delta E_{O\text{-}Vac}$) on the $Ce_{0.963}Pr_{0.037}O_2$(111) slab

Oxygen	$\Delta E_{O\text{-}Vac}$ (eV)
O1	0.98
O3	0.97
O4	0.99
O6	1.06

Table 3. Calculated distances from selected cations to O1 and O1-hole sites, for the 3.7 at% Pr-doped CeO_2(111) slab with and without O1-defect

Slab	Site	Site–Cation distance (Å)		
		Ce1	Ce3	Pr
$Ce_{0.963}Pr_{0.037}O_{2-x}$(111) (O1-defect)	O1-hole	2.63	2.54	2.62
$Ce_{0.963}Pr_{0.037}O_2$(111)	O1	2.38	2.36	2.43
Distance difference, (%)		9.7	7.0	7.3

Table 4. Undoped and Pr-doped CeO_2(111) slabs with a dioxygen (O_U–O_L) species adsorbed on different O-hole sites. Calculated distances from the lower O (O_L) to its coordinated cations.

Slab	Site	Site–Cation distance (Å)		
		Ce1	Ce3	Ce9
O_2/CeO_{2-x}(111) (O_2/O1-hole)	O_L	2.46	2.74	2.44
CeO_2(111)	O1	2.39	2.39	2.39
Distance difference, (%)		2.93	14.64	2.09
		Ce1	Ce3	Pr
O_2/$Ce_{0.963}Pr_{0.037}O_{2-x}$(111) ($O_2$/O1-hole)	O_L	2.59	2.84	2.78
$Ce_{0.963}Pr_{0.037}O_2$(111)	O1	2.38	2.36	2.43
Distance difference, (%)		8.71	20.34	14.40
		Ce3	Ce4	Ce5
O_2/$Ce_{0.963}Pr_{0.037}O_{2-x}$(111) ($O_2$/O3-hole)	O_L	2.84	2.61	2.80
$Ce_{0.963}Pr_{0.037}O_2$(111)	O3	2.41	2.38	2.38
Distance difference, (%)		17.84	8.66	17.65
		Ce5	Ce8	Pr
O_2/$Ce_{0.963}Pr_{0.037}O_{2-x}$(111) ($O_2$/O4-hole)	O_L	2.58	2.58	3.12
$Ce_{0.963}Pr_{0.037}O_2$(111)	O4	2.41	2.41	2.35
Distance difference, (%)		7.05	7.05	32.77
		Ce2	Ce5	Ce6
O_2/$Ce_{0.963}Pr_{0.037}O_{2-x}$(111) ($O_2$/O6-hole)	O_L	2.60	2.78	2.84
$Ce_{0.963}Pr_{0.037}O_2$(111)	O6	2.38	2.39	2.39

Distance difference, (%)	9.24	16.32	18.83

Table 5. Adsorbed dioxygen (O_U–O_L) species on CeO_{2-x}(111) and $Ce_{0.963}Pr_{0.037}O_{2-x}$(111) slabs: computed adsorption energy (ΔE_{O2-Ads}) and meaningful parameters values.

Slab	Adsorption Site	ΔE_{O2-Ads} (eV)	O_U–O_L Distance (Å)	Bader Charge	Spin Magnetization (μB)	Estimated Oxidation State	ν_{O-O}, (cm^{-1})	Formed Species
CeO_{2-x}(111)	O1-hole	–1.49	1.45	13.19	0	–2.00	901	(O_2^{2-})
$Ce_{0.963}Pr_{0.037}O_{2-x}$(111)	O1-hole	–1.00	1.34	12.75	–0.81	–1.26	1108	(O_2^-)
	O3-hole	–1.23	1.34	12.74	–0.88	–1.23	1131	(O_2^-)
	O4-hole	–1.21	1.36	12.80	0.89	–1.34	1063	(O_2^-)
	O6-hole	–1.20	1.34	12.73	–0.86	–1.20	1124	(O_2^-)

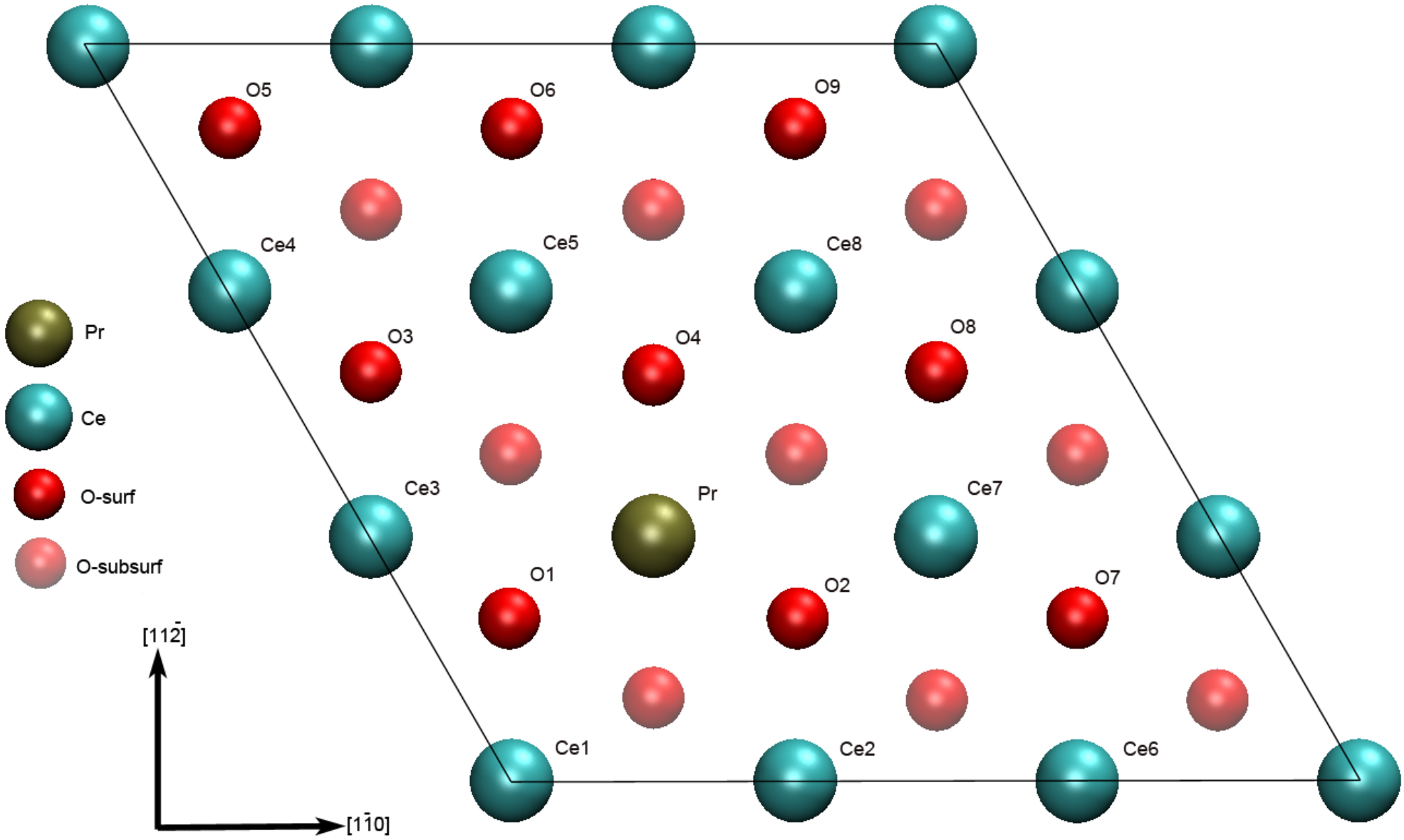
Pr
Ce
O-surf
O-subsurf
[11$\bar{2}$]
[1$\bar{1}$0]
O5
O6
O9
Ce4
Ce5
Ce8
O3
O4
O8
Ce3
Pr
Ce7
O1
O2
O7
Ce1
Ce2
Ce6

(a)

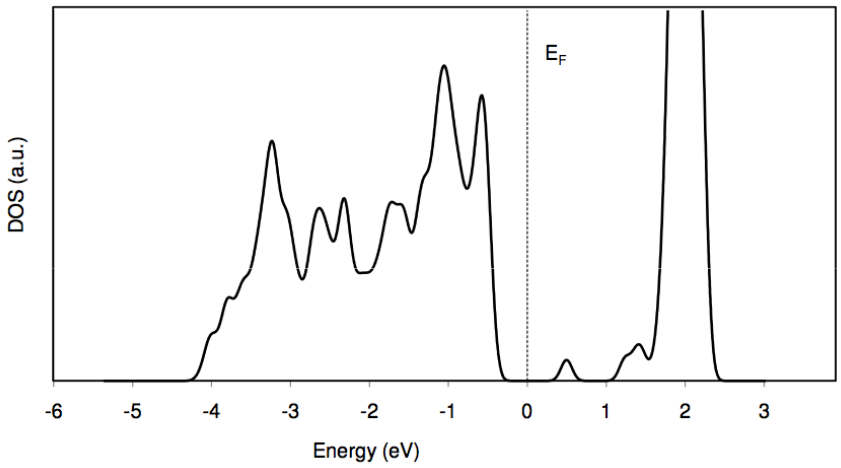

(b)

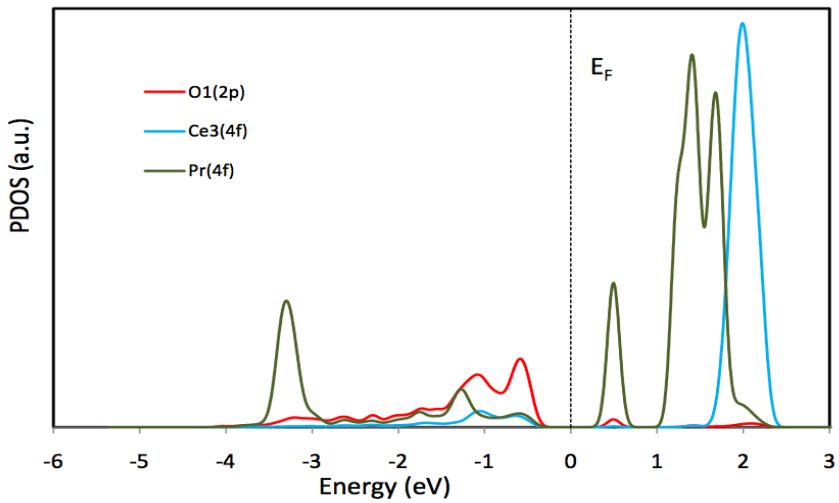

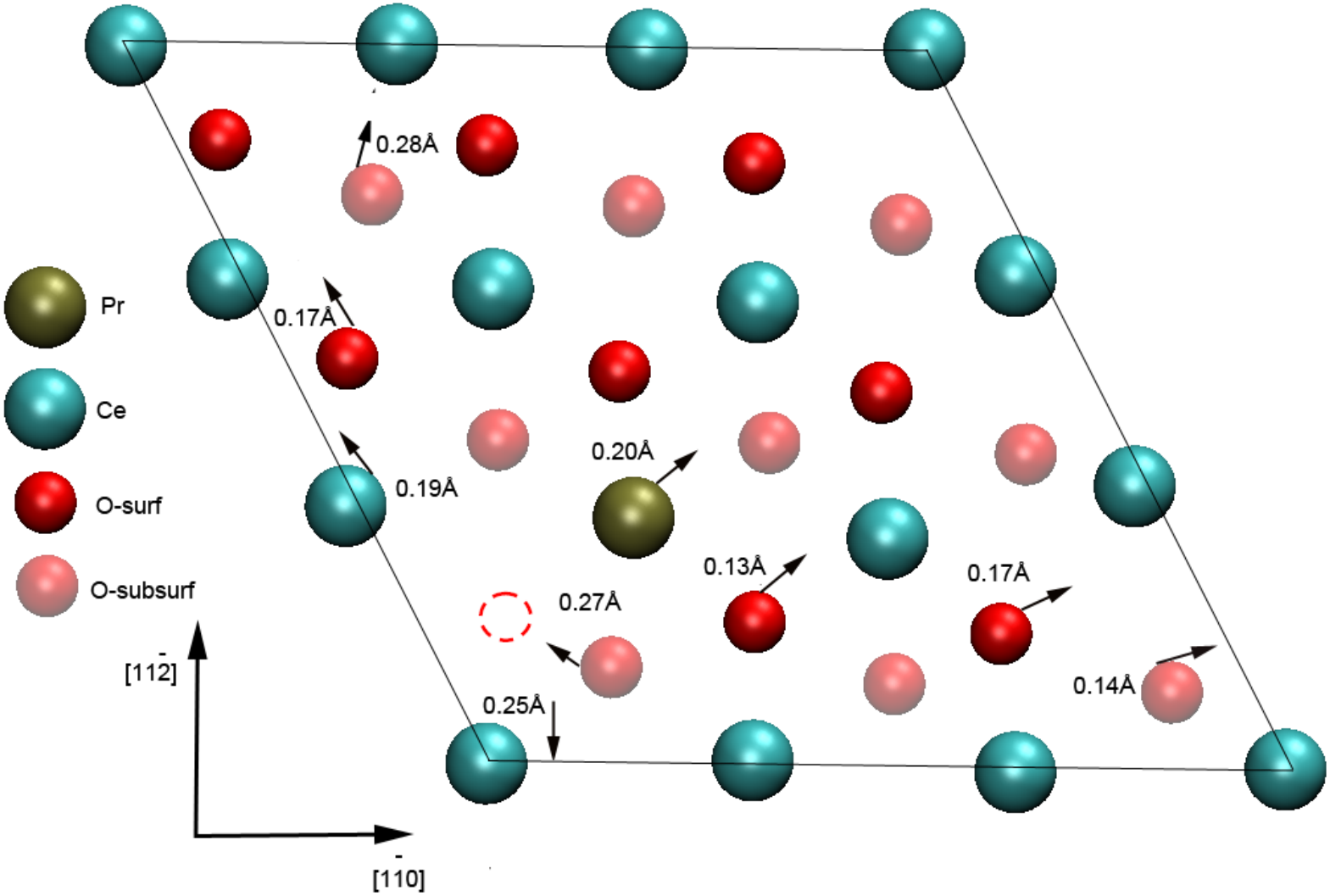

(a)

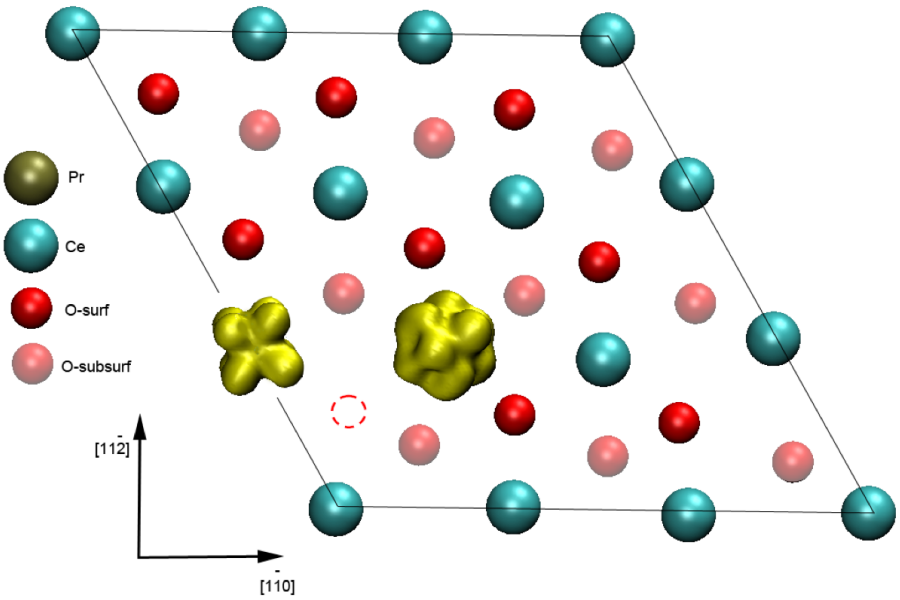

(b)

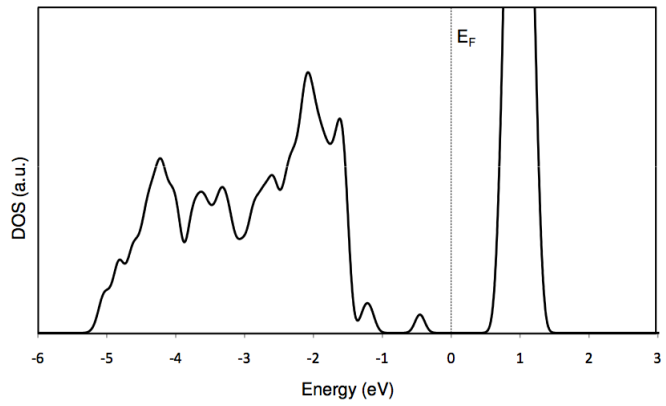

(c)

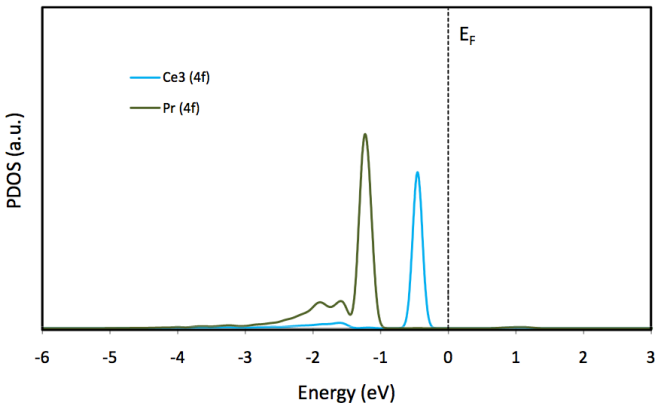

(a)

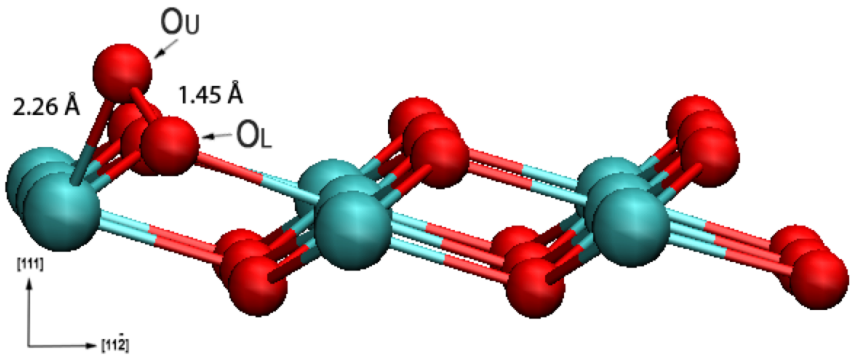

(b)

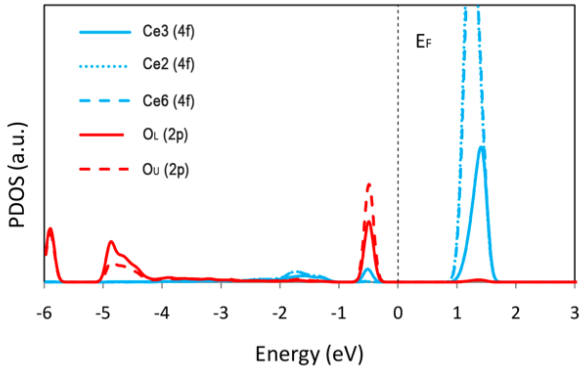

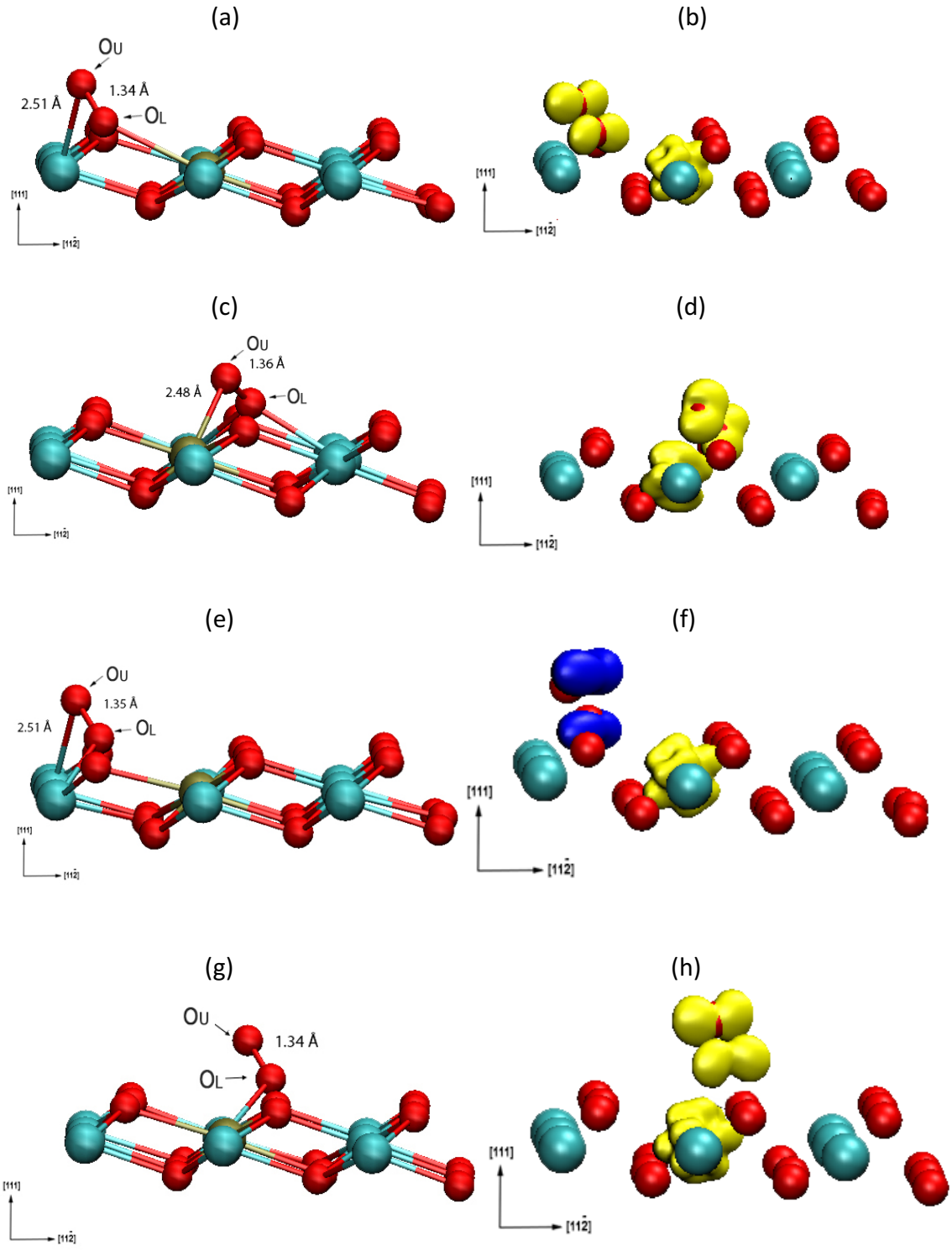

(a)

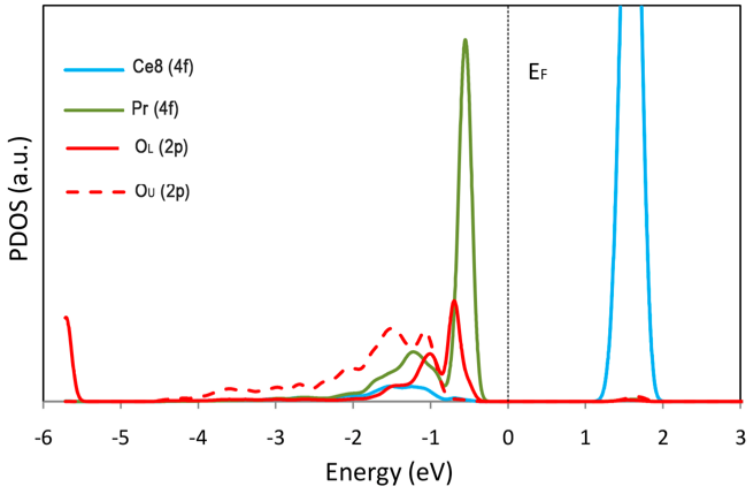

(b)

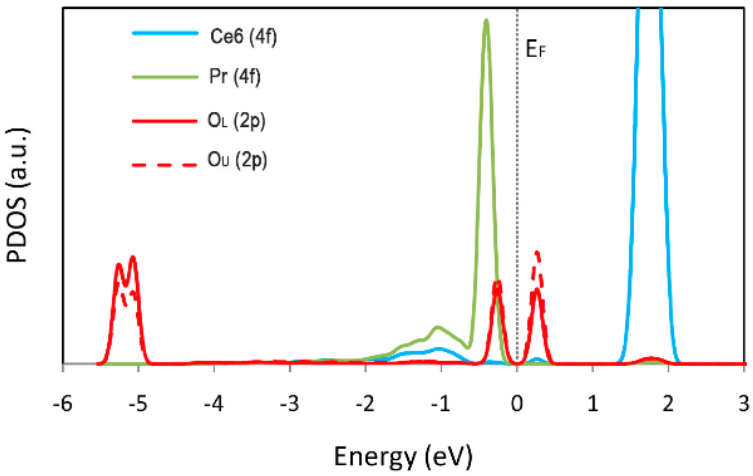

(a)

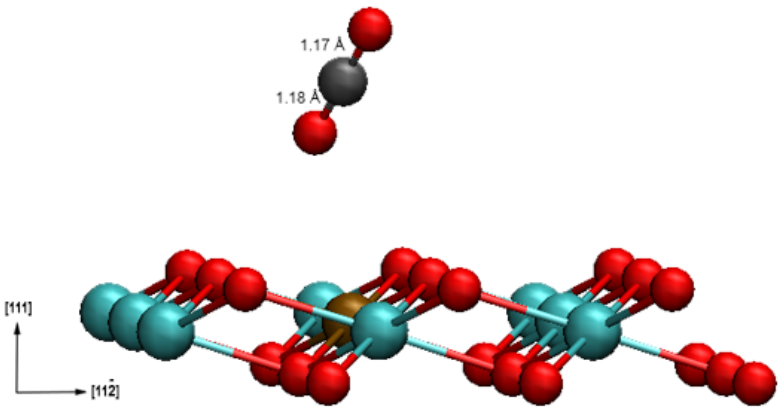

(b)

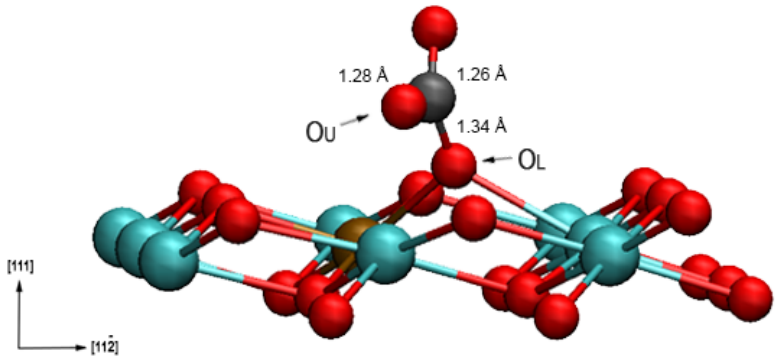

(c)